

RESEARCH ARTICLE

10.1029/2017JC013734

A Reconstruction Method for Hyperspectral Remote Sensing Reflectance in the Visible Domain and Applications

Zhaoxin Li¹, Deyong Sun^{1,2}, Zhongfeng Qiu^{1,2}, Hongyan Xi³, Shengqiang Wang^{1,2}, William Perrie⁴, Yunmei Li⁵, and Bing Han⁶

Key Points:

- We propose a new method to reconstruct hyperspectral R_{rs} using global multispectral measurements
- Ten reconstruction schemes are established; further assessments show that the eight-band scheme is optimal
- Ocean color remote sensing is shown to have high potential when the proposed method is applied to hyperspectral data

¹School of Marine Sciences, Nanjing University of Information Science & Technology, Nanjing, China, ²Jiangsu Research Center for Ocean Survey Technology, NUIST, Nanjing, China, ³Alfred Wegener Institute, Helmholtz Centre for Polar and Marine Research, Bremerhaven, Germany, ⁴Fisheries and Oceans Canada, Bedford Institute of Oceanography, Dartmouth, NS, Canada, ⁵Jiangsu Center for Collaborative Innovation in Geographical Information Resource Development and Application, Key Laboratory of Virtual Geographic Environment of Ministry of Education, College of Geographic Science, Nanjing Normal University, Nanjing, China, ⁶National Ocean Technology Center, State Oceanic Administration, Tianjin, China

Correspondence to:

Z. Qiu,
zhongfeng.qiu@nuist.edu.cn

Citation:

Li, Z., Sun, D., Qiu, Z., Xi, H., Wang, S., Perrie, W., et al. (2018). A reconstruction method for hyperspectral remote sensing reflectance in the visible domain and applications. *Journal of Geophysical Research: Oceans*, 123, 4092–4109. <https://doi.org/10.1029/2017JC013734>

Received 22 DEC 2017

Accepted 30 MAR 2018

Accepted article online 6 APR 2018

Published online 28 JUN 2018

Abstract

A reconstruction method was developed for hyperspectral remote sensing reflectance (R_{rs}) data in the visible domain (400–700 nm) based on in situ observations. A total of 2,647 R_{rs} spectra were collected over a wide variety of water environments including open ocean, coastal and inland waters. Ten schemes with different band numbers (6 to 15) were tested based on a nonlinear model. It was found that the accuracy of the reconstruction increased with the increase of input band numbers. Eight of these schemes met the accuracy criterion with the mean absolute error (MAE) and mean relative error (MRE) values between reconstructed and in situ R_{rs} less than 0.00025 sr^{-1} and 5%, respectively. We chose the eight-band scheme for further evaluation because of its decent performance. The results revealed that the parameterization derived by the eight-band scheme was efficient for restoring R_{rs} spectra from different water bodies. In contrast to the previous studies that used a linear model with 15 spectral bands, the nonlinear model with the eight-band scheme yielded a comparable reconstruction performance. The MAE and MRE values were generally less than 0.00016 sr^{-1} and 3% respectively; much lower than the uncertainties in satellite-derived R_{rs} products. Furthermore, a preliminary experiment of this method on the data from the Hyperspectral Imager for the Coastal Ocean (HICO) showed high potential in the future applications for reconstructing R_{rs} spectra from space-borne optical sensors. Overall, the eight-band scheme with our nonlinear model was proven to be optimal for hyperspectral R_{rs} reconstruction in the visible domain.

1. Introduction

Remote sensing reflectance (R_{rs}, sr^{-1}), which is approximately a function of both the absorption and back-scattering coefficients of the water optical constituents, is generally defined as the ratio of the water-leaving radiance to the downwelling irradiance just above the water surface. As one of the most important ocean color parameters, R_{rs} has been widely used to retrieve concentrations of chlorophyll-*a* (Chl-*a*), total suspended material (TSM) and colored dissolved organic matter (CDOM) (Moisan et al., 2011; Qiu, 2013; Siswanto et al., 2011; Zhang et al., 2017). The inherent optical properties (IOPs) of the optically active constituents (OACs) can also be efficiently retrieved by R_{rs} data, mainly in the visible domain (Lee et al., 2002). With the development of satellite sensors, currently there are numerous satellite products for various ocean color parameters with large spatial and temporal coverage, based on satellite-derived R_{rs} data (IOCCG, 1999). Therefore, it is crucial to acquire R_{rs} data with high accuracy and spectral integrity without losing important optical information in order to sufficiently represent the actual water optical conditions.

However, due to limitations of technology and high costs, most ocean color sensors have been multispectrally designed in the visible range, e.g., the Coastal Zone Color Scanner (CZCS), the Sea-Viewing Wide Field-of-View Sensor (SeaWiFS), the Moderate-Resolution Imaging Spectrometer (MODIS), the Medium Resolution Imaging Spectrometer (MERIS), and Sentinel-3 Ocean and Land Color Instrument (OLCI). A few hyperspectral sensors have been or will be designed, such as the Hyperspectral Imager for the Coastal Ocean (HICO, 2011–2015) (Lucke et al., 2011) and the upcoming hyperspectral missions –

Plankton-Aerosol-Clouds-Ecosystems (PACE), Environmental Mapping and Analysis Program (EnMAP) (Guanter et al., 2015), Hyperspectral Infrared Imager (HyspIRI) (Lee et al., 2015), etc. Although the bands of the currently existing sensors onboard these satellites have been designed to be capable of retrieving the optical characteristics of water surfaces, optical data from multispectral sensors can still not provide adequate information on the surface layer of water body compared with hyperspectral observations. Therefore, to enhance the capability for identifying various optical features of different OACs, it is important to acquire hyperspectral measurements. Here “hyperspectral” represents continuous spectral observations with a short spectral interval (≤ 5 nm) within a given spectral range. The scientific question is then whether the full spectral information can be extracted from the available multispectral R_{rs} data, so that potential applications based on the reconstructed R_{rs} can be further implemented to satellite data.

A number of previous studies have focused on the relationship between spectral characteristics and data at given multi-bands intending to recapture information at more bands. By using principal component analysis (PCA), Mueller (1976) found that the first three principal components of the radiance spectra (422.5–692.5 nm, 5 nm interval) measured from waters off the Oregon coast could represent changes of the ocean color spectra. Consistent findings were reported by Sathyendranath et al. (1989), showing that the pigment inversion algorithms could yield nearly the same retrievals with observations at 6 bands in a range of 413.5–762.25 nm, compared to 32 bands in the New York Bight (Sathyendranath et al., 1994). Moreover, Flink et al. (2001) found that more than 96% of the variance of spectral measurements in two Swedish lakes could be well approximated by the first three principal components. Similar results were also demonstrated by means of empirical orthogonal functions (EOFs) (Craig et al., 2012; Lubac & Loisel, 2007; Tool & Siegel, 2001). Becker et al. (2005) and Dekker et al. (1992) suggested that 8 bands in the visible to NIR (near-infrared) region and 9 bands in the 500–800 nm range should contain the majority of the full spectral information for some cases, respectively. Mélin and Sclép (2015) applied an in-water bio-optical model to perform band shifting, successfully expressing R_{rs} at for a missing wavelength based on data at neighboring bands. These studies have clearly shown that radiometric data have strong interdependence among adjacent bands because of the signal overlap, implying that it is possible to construct R_{rs} at one position by a combination of data at other wavelengths.

Studies on how to reconstruct hyperspectral reflectance spectra using multispectral data were rarely reported until the 1990s. Spitzer and Wernand (1986) proposed a linear transformation method for retrieving the complete solar irradiance spectra (400–720 nm), followed by Wernand et al. (1997) that successfully reconstructed full reflectance spectra in the range 400–720 nm (20 nm interval) through multivariate linear regression analysis (MLRA), with utilization of the radiometric measurements in five bands (412, 492, 556, 620, and 672 nm) collected from the Dutch and Belgian coastal waters as well as the Strait of Dover. Lee et al. (2014) reconstructed hyperspectral R_{rs} spectra in the range of 400–700 nm (5 nm interval) using 15 specific bands with satisfactory precision based on a worldwide R_{rs} data set, echoing the finding that approximately 15 bands within the visible domain are adequate for retrieving optical signals in most coastal and oceanic waters (Lee & Carder, 2002; Lee et al., 2007). More recently, Sun et al. (2015) finetuned the parameterization derived by Lee et al. (2014) for the R_{rs} data (400–750 nm, 5 nm interval) collected in highly turbid/eutrophic inland waters which were absent in former studies. The results showed sufficient accuracy in both magnitudes and spectral shapes for restoring the diverse R_{rs} spectra in inland waters. Moreover, Sun et al. (2015) also verified the feasibility of using MERIS and MODIS bands for the R_{rs} reconstruction, indicating that the available bands on existing multispectral sensors may not be optimal for reconstructing full R_{rs} spectra in the visible domain.

Most of the aforementioned work was based on a linear model for reconstruction. However, the results indicated that, to a certain extent, larger errors tended to appear at the red bands (> 600 nm) due to under-sampling and the limitations of a linear model (Lee et al., 2014; Sun et al., 2015; Wernand et al., 1997). Although it is possible to improve the model performance with more input data, the number of the available bands in the visible domain is insufficient (less than 15) for most satellite-derived R_{rs} data. It is yet to be known whether there is an optimal scheme which requires less input bands but still restores maximum spectral information, and whether a nonlinear reconstruction model works better than the linear one. As a potential reference for future applications in ocean color remote sensing, the objective of this paper is to identify the band positions that are optimal for hyperspectral R_{rs} reconstruction in the visible domain by

Table 1
Summary of the In Situ Data Set Used in This Study

Source	Date	Samples
Lake Chaohu	Jun. 2009	30
Lake Dianchi	Sep., Dec. 2009	31
Lake Taihu	Apr. 2009/May, Aug. 2010/ May 2011	148
Three Gorges Reservoir	Aug. 2009	23
Offshore of Zhejiang Province	May 2016	15
South China Sea	Mar. 2017	20
Yellow Sea & East China Sea	Sep. 2003/ May, Nov. 2014/ Aug. 2015/Jul. 2016	198
SeaBASS ^a	1998–2015	2,182
	Total sample	2,647

^aData available at <http://seabass.gsfc.nasa.gov/> for detailed information of SeaBASS data set.

using a novel nonlinear model. Since remote sensed R_{rs} data are observed worldwide, the proposed reconstruction method is developed on the basis of a global R_{rs} data set allowing for applications to various water bodies.

2. Data and Methods

2.1. Field Measurements

In situ hyperspectral R_{rs} used in this study were collected from the SeaWiFS Bio-optical Archive and Storage System (SeaBASS) (Werdell & Bailey, 2002) and several cruises conducted in waters in China (summarized in Table 1). SeaBASS is a repository of in situ bio-optical data with the purpose of acquiring a data set of sufficient quality, volume and diversity to support scientific analyses. It is comprised of both voluntarily contributed and funded data, including the measurements of apparent optical properties (AOPs), IOPs, phytoplankton pigment concentrations and other related oceanographic and atmospheric data.

All of these data were contributed by investigators worldwide, covering the Pacific and the South Atlantic Oceans, the Arabian Sea, the Mediterranean Sea, and the Gulf of Mexico. Due to lack of observations in China's aquatic environments in SeaBASS, field hyperspectral R_{rs} measurements from several cruises conducted in the South China Sea, the East China Sea, the Yellow Sea, the Bohai Sea, and the inland waters of China were also included.

As the in situ R_{rs} both from the SeaBASS data set and from cruises were obtained using different measuring methods or optical instruments, including the ASD Field spectroradiometer (350–1,050 nm, 1.5 nm interval) and the Hyper-Profiler II (349.4–804.0 nm, 3.3 nm interval), it is necessary to preprocess and unify the data. For the remote sensing reflectance measured just beneath the water surface (r_{rs} , sr^{-1}), we applied the water-air interface transfer formula to convert r_{rs} to R_{rs} based upon a semi-empirical relationship as expressed in Eq. (1) (Lee et al., 1998, 1999). We focused on the R_{rs} data in the visible domain of 400–700 nm in this study due to the fact that in both ultraviolet (UV) and NIR bands noise may occur and overwhelm the spectral information (Lee et al., 2013). In order to capture the information of the original spectra as much as possible and ensure the data quality, the R_{rs} spectra were all resampled into 1 nm resolution and smoothed with a 5-nm moving average filter to eliminate noise.

A total of 2,647 R_{rs} spectra representing different aquatic systems (Figure 1) were carefully selected on the global scale, covering blue clear waters in open oceans, blue to green (even yellow/brown) coastal waters and highly turbid waters. The concentrations of Chl-*a* and TSM ranged from 0.02 to over 100 $mg\ m^{-3}$ and 1 to over 100 $g\ m^{-3}$, respectively. Due to more complex water constituents and anthropogenic influences, the mean concentrations of Chl-*a* and TSM were 30.2 $mg\ m^{-3}$ and 49.7 $g\ m^{-3}$ respectively for turbid inland waters, which were much higher than those of most sea waters ($< 1.0\ mg\ m^{-3}$ for Chl-*a* and $< 5\ g\ m^{-3}$ for TSM).

$$R_{rs} \approx \frac{0.5r_{rs}}{1-1.5r_{rs}} \quad (1)$$

2.2. Remotely Sensed Data

One scene of HICO image for the area of the Yellow River estuary (19 August 2013) was obtained from the Earth Observing System Data and Information System (EOSDIS: earthdata.nasa.gov). Figure 2a shows the HICO true color image covering more than 8,000 km^2 with a spatial resolution of approximately 90 m. Hyperspectral atmospheric corrections were processed using the Level-2 generator (L2GEN) distributed in the SeaWiFS Data Analysis System (SeaDAS, version 7.4) (Ibrahim et al., 2018). Figure 2b shows the corresponding distribution map of Chl-*a* retrieved by the Ocean Color Index (OCI) algorithm (Hu et al., 2012). The reconstruction method was applied to HICO measured R_{rs} data within the range of 400–700 nm with 5.7 nm interval (52 bands) to preliminarily test its feasibility in satellite remote sensing data.

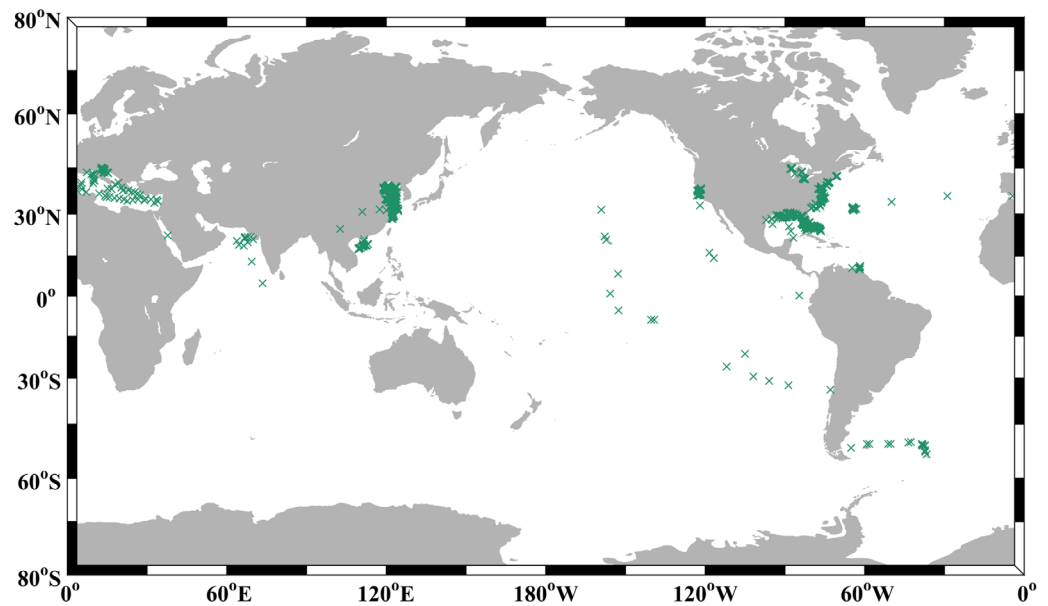


Figure 1. Geographic distribution of in situ data set used in this study.

2.3. Description of Reconstruction Models

In a linear model, R_{rs} reconstruction in a specific wavelength is expressed as

$$R_{rs}^{rc}(\lambda_j) = \sum_{i=1}^M K_{ij} R_{rs}(\lambda_i) \quad (2)$$

where the superscript rc means reconstruction and K_{ij} denotes empirical coefficient for the i -th input $R_{rs}(\lambda_i)$ toward the j -th output $R_{rs}^{rc}(\lambda_j)$. M represents the total input band number. Due to the insufficient

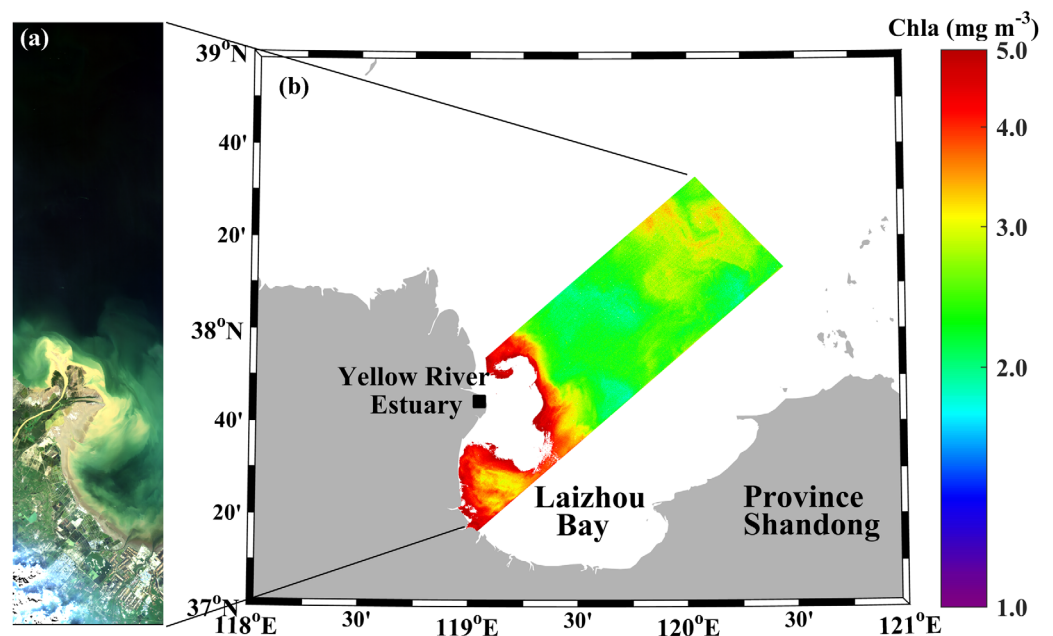


Figure 2. (a) True color image of HICO within the area of the Yellow River estuary of China (composite of HICO bands 42, 27 and 11) on Aug 19, 2013. (b) Distribution of chlorophyll- a concentration derived from OCI algorithm.

interpretation ability for the linear model for R_{rs} reconstruction in the red bands, a nonlinear method was proposed in this study

$$\ln [R_{rs}^{rc}(\lambda_j)] = \sum_{i=1}^M K_{ij} \ln [R_{rs}(\lambda_i)] \quad (3)$$

In order to avoid unnecessary calculation errors during the process of multivariate nonlinear regression, we further reformulated Eq. (3) as:

$$R_{rs}^{rc}(\lambda_j) = \exp \left\{ \sum_{i=1}^M K_{ij} \ln [R_{rs}(\lambda_i)] \right\} \quad (4)$$

If no special explanation is given, the model (or logarithmic model) mentioned hereafter refers to Eq. (4).

2.4. Establishment of Reconstruction Schemes

Due to limited priori knowledge, it is difficult to determine the bands that possess better capability for capturing spectral signatures. Although the method of PCA or EOF can diagnose the representative features of R_{rs} spectra in terms of several eigenvalues, the most significant bands for reconstruction are still unknown. However, a spectral analysis approach proposed by Lee et al. (2007) on the dominant band locations of signatures using derivative analysis can be taken as a reference to solve this problem. Derivative analysis plays an important role in enhancing the spectral features of hyperspectral measurements and thus has been widely used in many of the relevant studies (Becker et al., 2005; Holden & Ledrew, 1998; Tsai & Philpot, 1998; Wang et al., 2016; Xi & Zhang, 2011; Xi et al., 2015). Commonly used first and second derivative transformations are expressed in Eq. (5) and Eq. (6):

$$\left. \frac{dR_{rs}}{d\lambda} \right|_i \approx \frac{R_{rs}(\lambda_j) - R_{rs}(\lambda_i)}{\Delta\lambda} \quad (\Delta\lambda = \lambda_j - \lambda_i) \quad (5)$$

$$\frac{d^2R_{rs}}{d\lambda^2} = \frac{d}{d\lambda} \left(\frac{dR_{rs}}{d\lambda} \right) \quad (6)$$

Peaks and troughs in spectra showing the most significant signal changes can be located via derivative analysis, so that the bands that have the greatest possibility in capturing the changes of spectra can be identified as candidates for the reconstruction schemes. Based on all available in situ hyperspectral R_{rs} data in the range of 400–700 nm with 1 nm interval, we developed a 15-band scheme and established another nine schemes with less input bands. The detailed procedure for establishing the schemes is shown in Figure 3 and summarized as following:

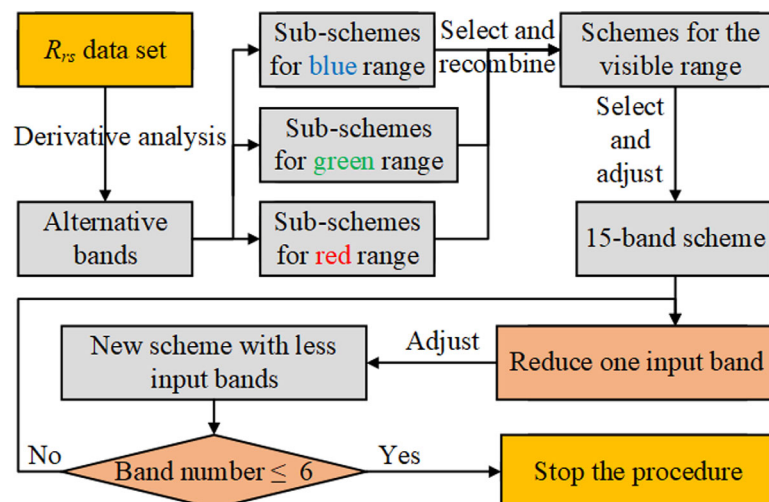


Figure 3. Flowchart of the procedure to establish the schemes.

1. We separated the full visible range into three sub-ranges, i.e., blue (400–499 nm), green (500–600 nm) and red (601–700 nm). In each sub-range, we chose five alternative bands to reconstruct R_{rs} spectra using the logarithmic model. The bands were derived using the equations (5) and (6). For instance, 412, 438, 449, 459, and 474 nm were selected as one possible sub-scheme and used to reconstruct R_{rs} data in the blue range, similarly 507, 534, 554, 581, and 593 nm for the green range, and 601, 615, 635, 677, and 698 nm for the red range.
2. When all the possible sub-schemes were tested, we chose those with the better performance for further recombination. In this case, the numbers of the bands for selected sub-schemes were 5, 5, and 3 for blue, green, and red sub-ranges, respectively. Hence, a total of 75 possible schemes were used to extract R_{rs} spectra in 400–700 nm.
3. The first reconstruction scheme consisted of the best 15 new bands that were selected from the 75 schemes. In order to maintain the reconstruction performance but take into account as few bands as possible, we tried to remove one band from the 15 bands and used the remaining 14 bands for reconstruction.
4. By evaluating the errors, we removed the band which was least sensitive to the reconstruction and two bands on both sides of that position were shifted to be closer to each other, in order to construct the second scheme with 14 bands.
5. Step (4) was repeated until the six-band scheme was established.

Note that the bands using in the first schemes were not exactly the same as those candidates in step (1) because adjustments had to be made on the bands around the joints of sub-ranges.

2.5. Evaluation Methods and Accuracy Criterion

To evaluate the performance of the reconstruction method described above, the mean absolute error (MAE) and mean relative error (MRE) between the measured R_{rs}^{true} and reconstructed R_{rs}^{rc} were calculated for all the 301 bands (400–700 nm with 1 nm interval) as below:

$$MAE(\lambda_j) = \frac{1}{N} \sum_{i=1}^N \left| R_{rs}^{rc}(\lambda_j) - R_{rs}^{true}(\lambda_j) \right| \quad (7)$$

$$MRE(\lambda_j) = \frac{1}{N} \sum_{i=1}^N \left| \frac{R_{rs}^{rc}(\lambda_j) - R_{rs}^{true}(\lambda_j)}{R_{rs}^{true}(\lambda_j)} \right| \times 100\% \quad (8)$$

Where the collected and well processed R_{rs} measurements were taken as proxies of “ground truth” with the superscript *true*. The subscript *i* and *j* mean *i*-th in situ spectrum and *j*-th reconstructed band, respectively. *N* is the total number of R_{rs} measurements in the data set. Besides the MAE and MRE, the correlation coefficients (R^2) for each parameterization were also calculated. The median absolute percent difference (MPD) was defined in Eq. (9) to quantify the difference between the satellite-derived R_{rs}^{sat} and reconstructed R_{rs}^{rc} at *j*-th pixel of the observed area (λ_j means *j*-th output band):

$$MPD_j = median \left| \frac{R_{rs}^{rc}(\lambda_j) - R_{rs}^{sat}(\lambda_j)}{R_{rs}^{sat}(\lambda_j)} \right| \times 100\% \quad (9)$$

However, the error in the reconstructed R_{rs} spectra deemed to be acceptable was yet to be defined. It was thus necessary to determine a criterion that could preliminarily assess whether the band setting was sufficiently accurate for the reconstruction scheme procedure. According to previous studies involving satellite-derived R_{rs} data (Hooker & Esaias, 1993; Hu et al., 2013; Qi et al., 2017), the objective accuracy criterion introduced in the present study was that the MRE and MAE at every output band must be within 5% and 0.00025 sr^{-1} , respectively, for the whole visible range. These thresholds were set according to the fact that the uncertainties of satellite-retrieved R_{rs} for blue bands over clear waters had been widely accepted to be within 5%, while R_{rs} uncertainties (in %) in longer bands were significantly higher under the same aquatic conditions. Moreover, the MODIS- and SeaWiFS-derived R_{rs} uncertainties were nearly 0.00025 sr^{-1} in green-red bands, which were smaller than those in blue bands for oligotrophic waters ($\text{Chl-}a < 0.1 \text{ mg m}^{-3}$) by a factor of two (Gordon, 1997; Hu et al., 2013).

3. Results

3.1. Variability of R_{rs} Spectra

Figure 4a exhibits examples of R_{rs} spectra to emphasize the large variability in both magnitudes and spectral shapes. Figure 4b shows the corresponding mean R_{rs} , standard deviation (SD), and coefficient of variation (CV, defined as the standard deviation divided by the mean) for all R_{rs} spectra. CV varied approximately from 100% in the shorter bands to 200% in bands above 500 nm, implying a significant variation throughout all bands, especially the green-red bands. The R_{rs} measurements from blue oceanic waters showed relatively lower values and monotonically decreasing spectral shape in the range of 400–700 nm. Note that the values close to zero at bands beyond 600 nm were critical due to the strong absorption of pure water in the red bands (Pope & Fry, 1997). The R_{rs} spectra with higher magnitudes and more variation in spectral shapes typically represented optically-complex waters, with strong impact of the absorption of phytoplankton and CDOM in blue bands, the backscattering of particulate sediments near green bands, the Chl-*a* fluorescence near 680 nm (Gordon, 1979; Pope & Fry, 1997), and possibly the bottom effects (Lee et al., 1998, 1999).

It is well acknowledged that the oceanic bio-optical variables are approximately log-normally distributed (Campbell, 1995). It is thus reasonable to assume that R_{rs} data also obey the lognormal model (Matsuoka et al., 2016). Figure 5 shows the frequency of natural log-transformed R_{rs} averaged with respect to wavelengths. The mean and standard deviation of its fitting to a Gaussian function curve was -5.7 and 1.05 , passing the *t*-test with a confidence level of 95%. This distribution was a combination of different kinds of R_{rs} spectra from various water types. The small peak around -3.5 was attributable to highly turbid waters with mean R_{rs} close to 0.03 sr^{-1} . It is noteworthy that the lognormal distribution was more standard if R_{rs} data only represent the same water body. Nevertheless, the lognormal distribution of large data set of R_{rs} data provided the basis for the reconstruction model shown in Eq. (4).

3.2. Reconstruction Schemes

Spectral derivative analysis is able to eliminate background interference and distinguish overlapping signatures between neighboring bands. Mathematically, the band where the first-order derivative becomes zero corresponds to the existence of an extreme value (peak or trough) of an R_{rs} spectrum, whereas second-order derivative equal to zero pinpoints the spectral inflection. Both of these zeroes indicate the exact locations where important signal information of R_{rs} exist. The distributions of the frequency where the first- and second-order derivatives equal to zero are shown in Figure 6, where higher frequency value indicated more important spectral information at the corresponding band. A total of 35 alternative input bands were diagnosed. Finally, ten reconstruction schemes, notated as S01 to S10, were established by following the above mentioned procedure (Figure 3), with the band number decreasing from 15 to 6 (Table 2). The performance of each scheme was assessed below by statistically comparing the reconstructed R_{rs} to the in situ ones.

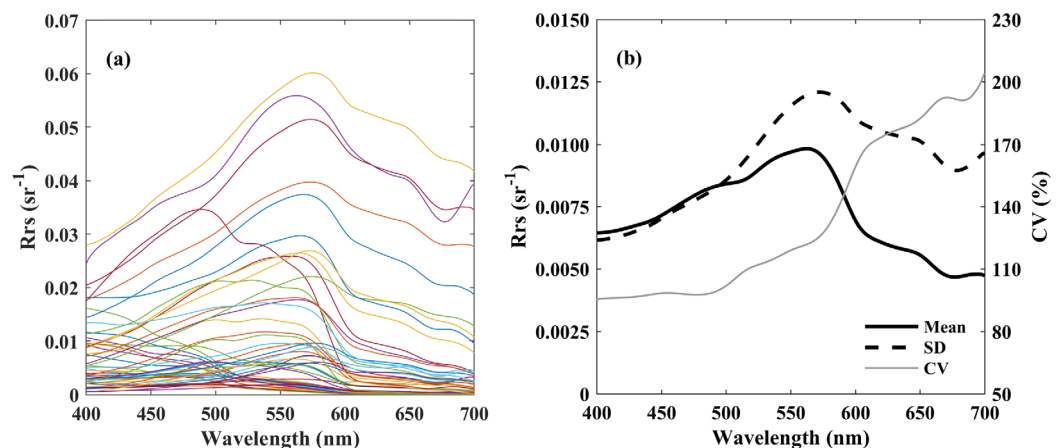


Figure 4. (a) Examples of measured R_{rs} spectra used in this study. (b) Mean, standard deviation (SD), and coefficient of variation (CV) of the whole R_{rs} data set.

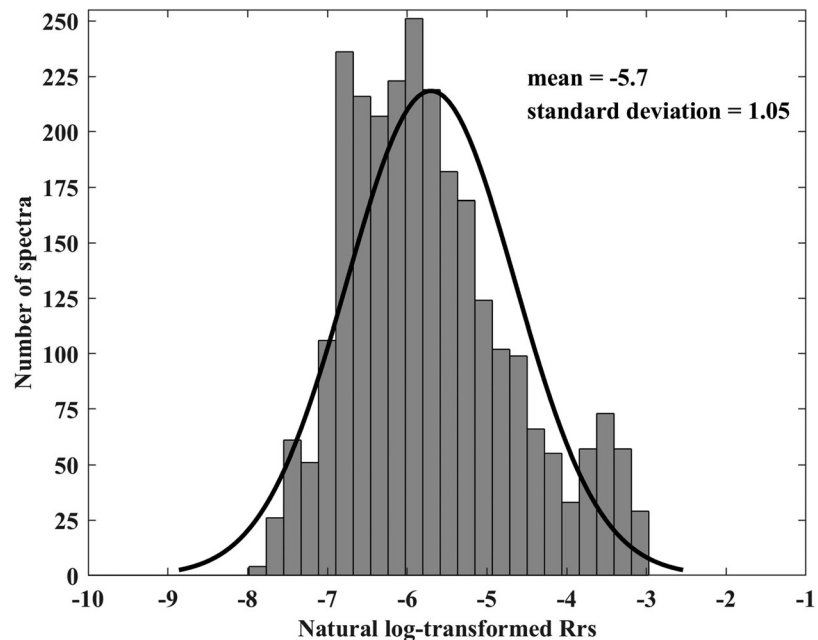


Figure 5. Histogram showing frequency of natural log-transformed R_{rs} averaged on wavelengths. Black line shows the corresponding normal distribution with mean and standard deviation.

3.3. Reconstructed Hyperspectral R_{rs}

Upon development of the logarithmic model, we randomly selected 80% of the total spectra ($N = 2,118$, namely main data set) for assessing schemes S01–S10. Figures 7a–7c) shows the MAE, MRE and R^2 values in each band (x-axis) of each scheme (y-axis). Remarkably, the logarithmic model showed satisfactory results, with most schemes achieving the accuracy criterion except for S09 and S10. The MRE of S09 and S10 exceeded 5% at several red bands and MAE exceeded 0.00025 sr^{-1} at a few blue and green bands for S10. Most of the MAE and MRE for S01–S08 were generally $< 0.00012 \text{ sr}^{-1}$ and $< 3\%$, respectively, with R^2 ranging from 0.9965 to 1.0, except for the bands beyond 600 nm, especially from 650 to 700 nm, the MRE increased by about 1–2% compared to those of the shorter bands. In addition, the three statistical parameters were averaged over the entire output bands for each of the schemes S01–S10, as shown in Figures 7d–7f, to highlight the representative performance of each scheme. The results showed that the errors (MAE

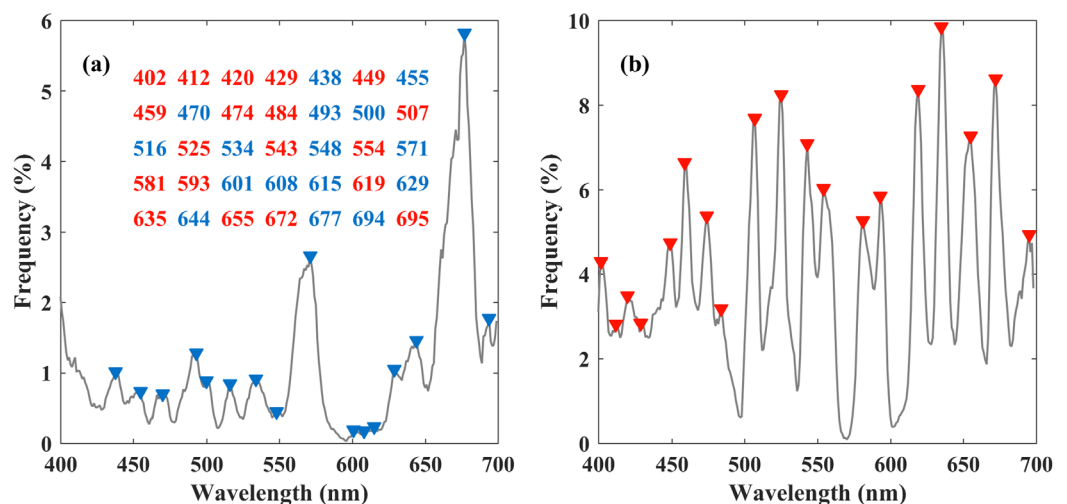


Figure 6. Frequency distribution of bands where the first-order (a) and second-order (b) derivatives of R_{rs} equal to zero. Triangle marks represent the positions of these bands (listed in blue for first-order and red for second-order derivatives).

Table 2
Band Placements for the Established 10 Reconstruction Schemes (S01-S10)

Band #	S01	S02	S03	S04	S05	S06	S07	S08	S09	S10
1	402	402	402	404	404	404	405	407	410	410
2	420	420	425	435	443	450	452	465	474	500
3	443	449	455	474	488	501	500	530	543	571
4	466	488	492	516	531	540	542	578	588	635
5	493	516	525	554	565	580	580	613	634	675
6	516	543	557	581	595	608	613	659	675	698
7	543	571	585	604	619	639	659	681	698	
8	571	593	606	629	650	663	681	698		
9	593	610	629	652	672	683	698			
10	610	629	652	672	687	698				
11	629	652	672	687	698					
12	652	672	687	698						
13	672	687	698							
14	687	698								
15	698									

units: nm

and MRE) were increasing and R^2 was decreasing relatively steadily from S01 to S10, despite of the relatively sharp changes observed from S07 to S08 and S09 to S10.

The remaining 20% of the data set ($N = 529$, namely validation data set) was used to validate the model regarding the derived K_{ij} matrices. Figure 8a presents the percentage of different ranges of MRE for each scheme, showing that the results from two data sets were in good agreement. These results suggested that the model was applicable for diverse R_{rs} spectra. Apparently, the predominant range of MRE was 0–1% for S01 to S03, 1–2% for S04 to S07, 2–3% for S08 to S09 and 4–5% for S10. High errors ($> 4\%$) were found in S09 and S10, where the MRE within 6–7% accounted for a majority. Figures 8b–8d exhibit the distributions of the model coefficients K between input and output bands for S01, S05 and S08 as examples, showing that the closer the i -th input and j -th output band are, the greater the K_{ij} value is. It means that the information of the reconstructed spectrum at one output band is mostly provided by the spectral values at adjacent bands since they are highly correlated.

3.4. Preliminary Application to HICO Data

To determine whether our method could work well for satellite remote sensing data, we conducted a preliminary experiment by directly applying the model expressed by Eq. (4) with the parameterization derived from S08 to HICO data. Since the required eight bands in S08 are not all available from the HICO data, instead, we used the closest eight bands of HICO to extract R_{rs} spectra, which are band 10 (404 nm), band 21 (467 nm), band 32 (530 nm), band 40 (576 nm), band 46 (610 nm), band 54 (656 nm), band 58 (679 nm), and band 61 (696 nm). Figure 9a shows that the majority of MPD values from HICO-derived and reconstructed R_{rs} results fell in the range of 3–6%. Higher reflectance near the coast resulted in lower MPD and vice versa. Figures 9b and 9c) shows that MAE and MRE results were generally under 0.0005 sr^{-1} and 5%, respectively. High discrepancies in the range 400–450 nm were caused by the unrealistic humps of atmospherically corrected R_{rs} data (Ibrahim et al., 2018), as the reconstruction scheme did not duplicate the errors from the atmospheric correction (Figure 9d). In general, the preliminary experiment on HICO data suggested that the proposed reconstruction scheme was promising for the future applications in optical sensors from space.

4. Discussion

In order to build up the new 15-band scheme based on our data set, both characteristic locations and data validity for modeling were considered, which made the procedure more practical for retrieving R_{rs} data at each output band. Compared to the proposed approach by Lee et al. (2014), the mean errors of S01 were generally about 0.25% higher in the range 420–520 nm, but about 1.0% lower in 600–700 nm (figures not shown), due to the fact that more input bands were considered in the red domain rather than the green or blue ranges. This configuration has brought many benefits indeed. Theoretically, the error at each output

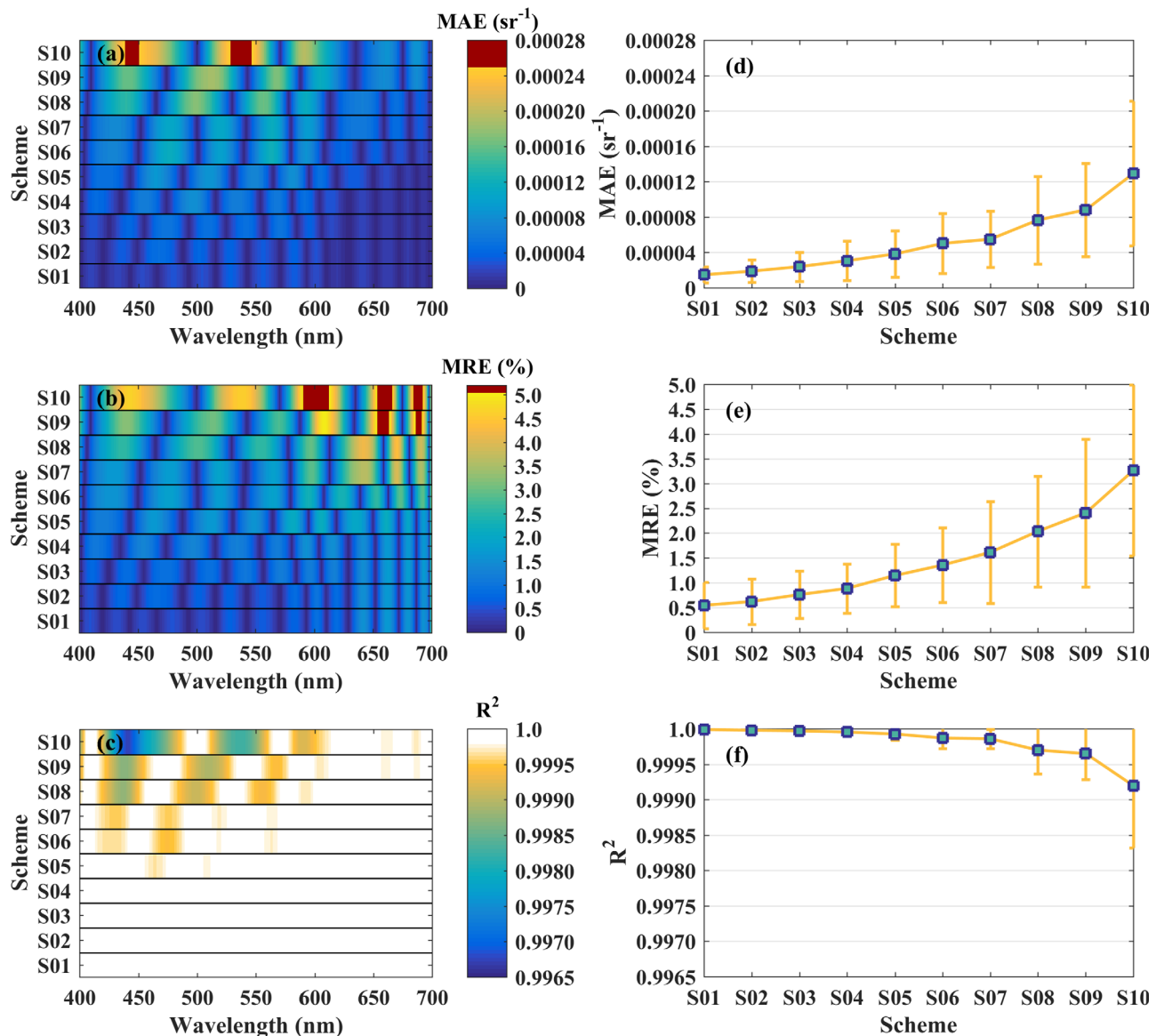


Figure 7. (a–c) Distributions of MAE, MRE and R^2 in 400–700 nm varied with schemes S1–S10 ($N = 2,118$); (d–f) Averaged MAE, MRE and R^2 upon band with SD for each scheme, respectively.

band was restrained by the two adjacent input bands, therefore the accuracy was lower when the scheme had fewer input bands which might result in sudden increase in MRE at the red bands (Figure 7b) and the variation patterns in Figures 7d–7f) in S10.

S01–S08 satisfy well the objective accuracy criterion introduced in this paper, although unexpectedly high errors appear in schemes S01–S10 at several bands. This suggests that with less than eight bands R_{rs} spectra may not be able to provide adequate spectral features to reconstruct hyperspectral R_{rs} with sufficient accuracy at each band. More channels of a sensor require more storage units onboard the satellite, demanding more financial expense and high technical support. A compromise between the accuracy and band number should be considered in order to determine an optimal scheme. The performance of S08 can be summarized as (1) the maximal MAE (MRE) was located around 500 (640) nm about 0.00016 sr^{-1} (4%), and (2) most of MRE values are between $\sim 0\%$ and 3%, accounting for $> 80\%$ of the total (Figure 8a). This implies that the coefficient matrix derived by S08 contains the majority of the typical spectral characteristics from our extensive data set. With the satisfactory accuracy and a minimum of required input bands, S08 was chosen as the optimal scheme for supplementary evaluation.

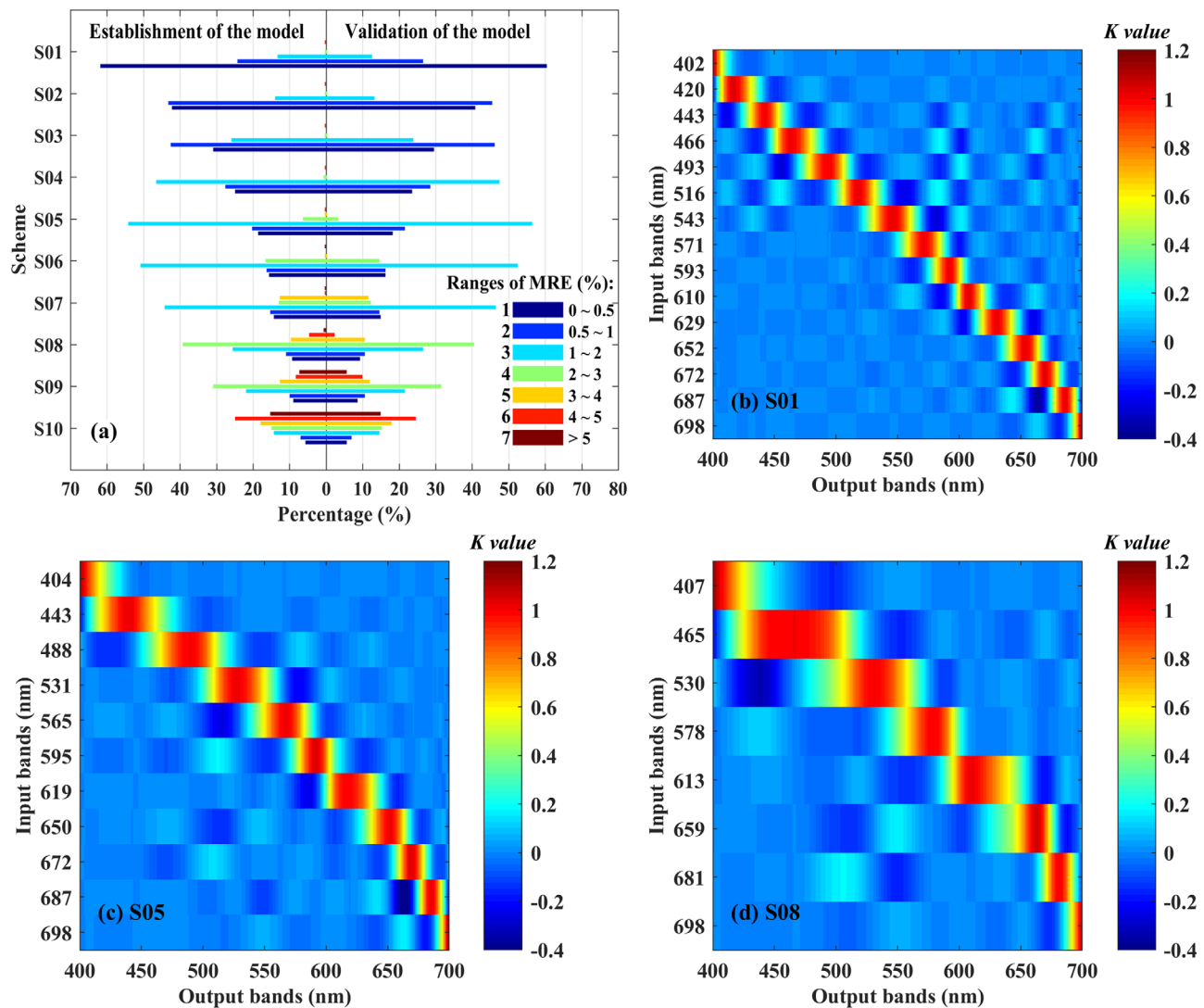


Figure 8. (a) Percentage of different ranges of MRE for the main data set ($N = 2,118$, left) and validation data set ($N = 529$, right). (b–d) The distribution of the model coefficients derived using Eq. (4) for S01, S05, and S08, respectively.

4.1. Assessment in Different Water Types

4.1.1. Simple Classification of Water Types

The above results showed a well reconstruction effect of the modeling with respect to the entire data set (namely overall modeling). However, the samples in the data set were collected from different water types. Does the reconstruction model fit for different separate water types? Or whether the performance is better if we establish reconstruction models for each water type (namely separate modeling)? For this purpose, we divided the data set into three classes. Firstly, a simple classification approach, $R_{rs}(440)/R_{rs}(550)$, was used to separate the samples collected in the ocean into two types, with the value ≥ 1.0 as Type 1 and < 1.0 as Type 2, respectively. The R_{rs} spectra from inland turbid waters were considered as Type 3. Figure 10a shows the scatterplots of $R_{rs}(440)$ versus $R_{rs}(550)$ for all the three types. Figure 10b displays the mean R_{rs} spectrum for each classification with corresponding standard deviation, representing general spectral shapes and magnitudes for the three water types. Particularly, the mean $R_{rs}(440)$ and $R_{rs}(550)$ in Type 3 are both over 4 times higher than that from Type 2 (mostly coastal waters), showing further the diversity of these water types, thus it is reasonable to exclude the inland turbid waters from Type 2 and regard them as another distinct classification. Note that the classification method used in this study is only to test and assess how the sensitivity of the reconstruction method varies on different water types; classified water types by this classification approach are not exhaustive.

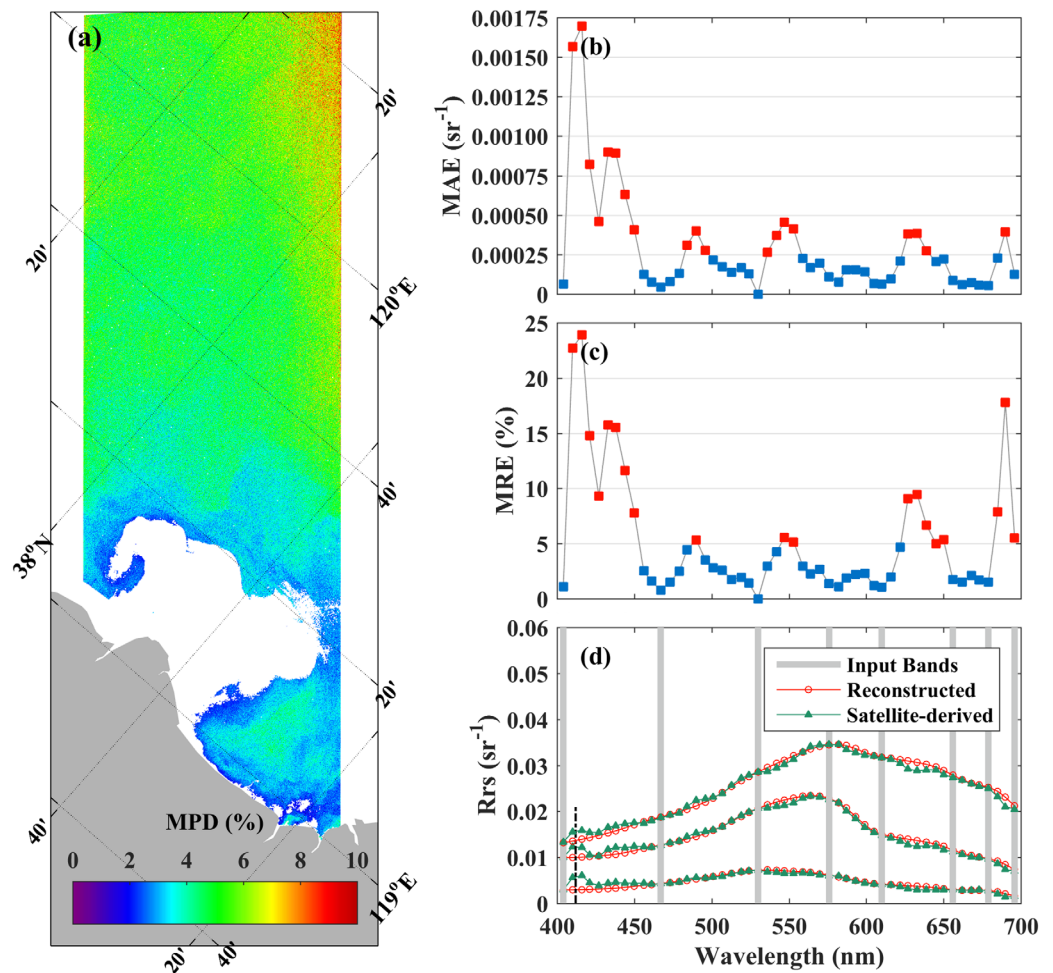


Figure 9. Distribution of (a) MPD, (b) MAE, (c) MRE, and (d) three selected pairs of HICO-derived and reconstructed R_{rs} spectra. The red square marks in (b) and (c) denote mean errors that are beyond the criterion, and the black dashed line in (d) indicates the position of the hump.

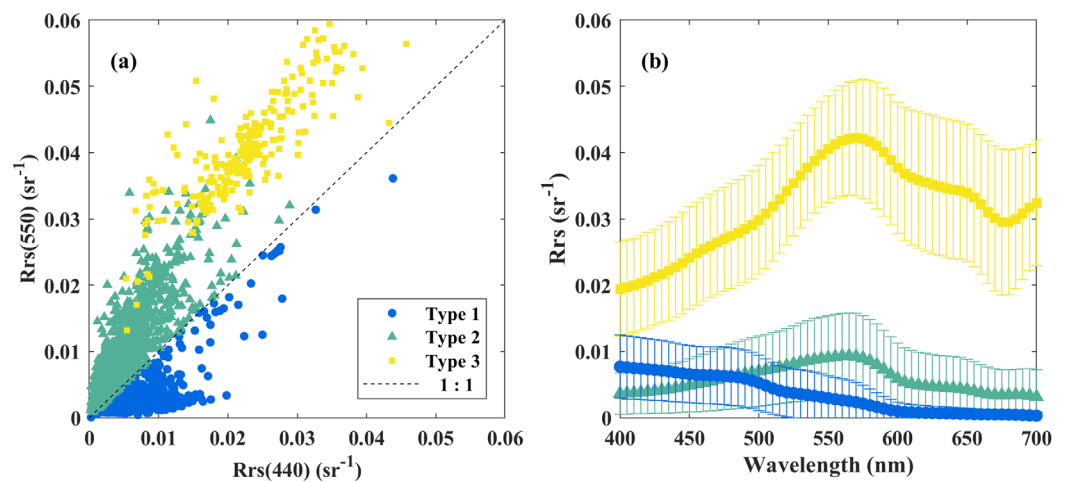


Figure 10. (a) Scatterplot of $R_{rs}(440)$ versus $R_{rs}(550)$ for the three water types. (b) The mean spectrum for each water type with the corresponding standard deviation.

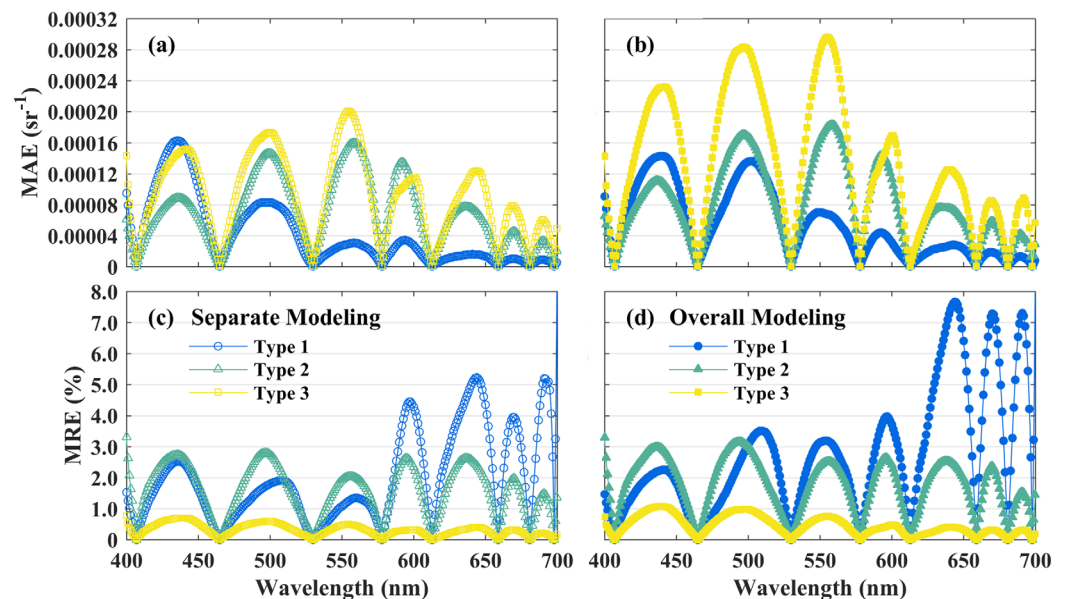


Figure 11. Distributions of MAE and MRE of the separate (a, c) and overall (b, d) modeling using S08 for waters based on validation data set.

4.1.2. Assessment for Reconstructions Based on Different Water Types

Three new coefficient matrices were finally determined, corresponding to respective spectral features for each water type (Type 1, 2 and 3). Figure 11 exhibits the distributions of MAE and MRE for S08 when applying separate and overall modeling to the validation data set (20% of each classified R_{rs} subset). For Type 1, the notable distinctions were found in MRE values around 600–700 nm between the separate and the overall modeling, because extremely low values in the red band of the R_{rs} in open ocean waters resulted in low MAE values but high MRE values (Werdell et al., 2013). The retrievals of the two modelings beyond 600 nm were thought to be equally effective, except that the errors of the overall modeling were slightly higher than those from the separate modeling in the green range. Interestingly, the accuracy of the overall modeling was in agreement with that of the separate modeling in Type 2. Whereas for Type 3, the peak of the amplitude for MAE in Figure 11b approached 0.0003 sr^{-1} near 560 nm, about 0.0001 sr^{-1} higher than the amplitude in Figure 11a in the blue-green range. It is not surprising due to the relatively higher spectral complexity in R_{rs} and fewer samples compared to that of Type 1 and Type 2. However, since the magnitude of mean R_{rs} spectrum for Type 3 was about 4 times higher than those in the other two types (Figure 10), the reconstruction accuracy of the overall modeling for highly turbid waters was acceptable (MRE < 1% at blue-green bands and < 0.5% at red bands). In conclusion, despite of a few exceptions, the accuracy criterion was generally met in the three water types for overall modeling. The coefficient matrix determined by the overall modeling using S08 in this study was proven suitable for open ocean and coastal waters, as well as China's inland turbid waters (see examples given in Figure 12).

4.2. Comparison With Other Methods

Previously, Lee et al. (2014) and Sun et al. (2015) both developed reconstruction methods for hyperspectral R_{rs} in the visible range using a linear model with the same 15 bands (C1 in Table 3) but a different data set. To test whether the reconstruction method using S08 with a logarithmic model was comparable to previously proposed methods, we applied the three coefficient matrices (namely, K_{S08} , K_{Lee} and K_{Sun} , respectively) directly to our data set, which covered the spectra used in those two studies. The evaluation and inter-comparison of the three approaches illustrated in Figure 13 showed that the errors from K_{Lee} and K_{Sun} were generally lower in the blue-green range compared with that of K_{S08} due to more input bands placed there, specially in 400–530 nm, where there were seven bands in C1 but only three in S08. The MAE and MRE were mainly within 0.00004 sr^{-1} and 1% respectively at the blue bands for K_{Lee} and K_{Sun} but less than 0.00016 sr^{-1} and 3% for K_{S08} . For the red bands, K_{Sun} performs poorly due to the lack of R_{rs} spectra from relatively clear waters (Type 1 or 2), leading to an inaccurate estimation, such as

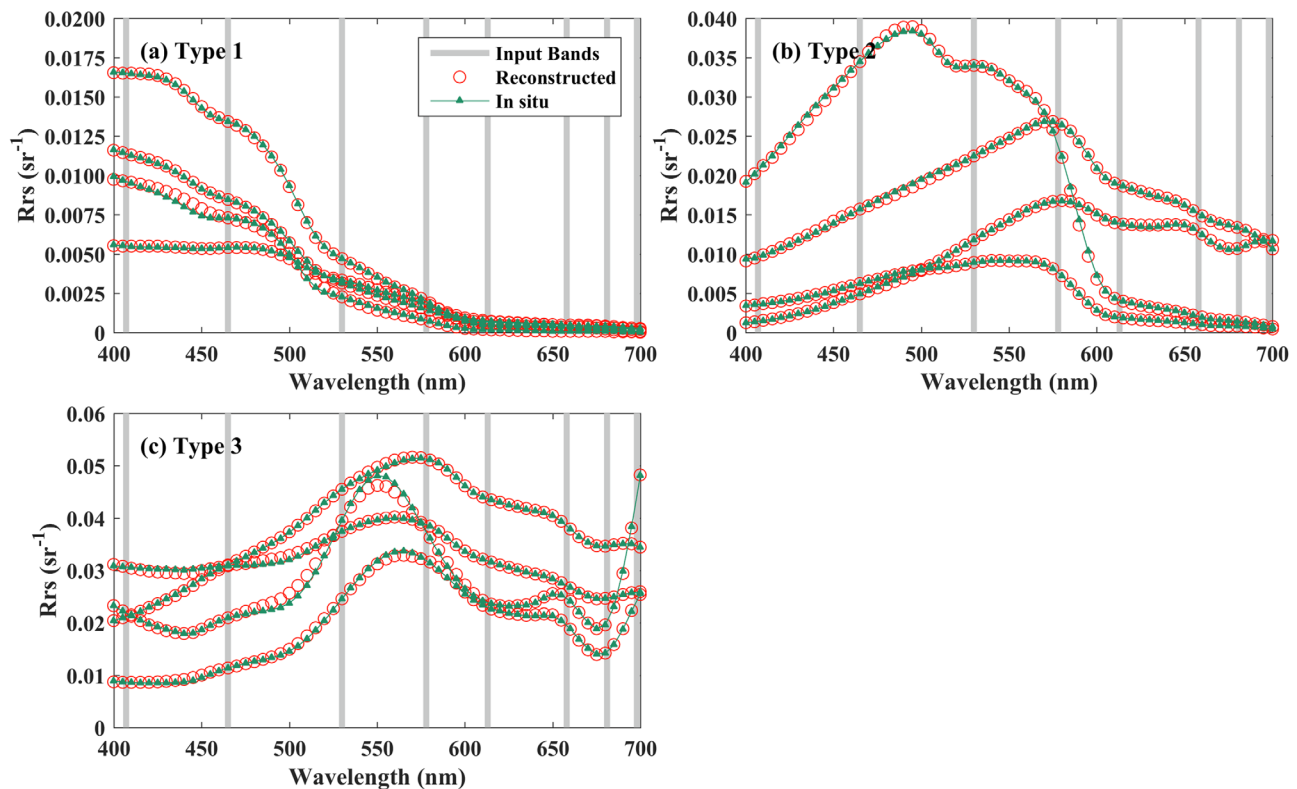


Figure 12. Four pairs of the reconstructed and in situ R_{rs} spectra in each water type selected from the validation R_{rs} data set for overall modeling using S08.

spectrum 1 in Figure 13d. However, the accuracy of K_{Lee} was comparable to that of K_{S08} within the range of 600–700 nm, where the MAE and MRE were $< 0.00008 \text{ sr}^{-1}$ and $< 4\%$ respectively, though there was one band less in S08 than that in C1. The restored spectra by the three methods showed a fine conformance to the in situ data, which was also reflected in the distribution of R^2 that approached 1.0. In summary, the utilization of the eight-band scheme and logarithmic model yielded comparable retrievals with less input bands, suggesting notable potential in future applications.

4.3. Logarithmic Model Versus Linear Model

It is difficult to reconstruct hyperspectral R_{rs} spectra in the red range due to the contributions of Chl-*a* absorption that causes a trough near 675 nm, and Chl-*a* fluorescence that causes an abrupt reflectance peak near 685 nm. A linear model with $R_{rs}(\lambda)$ at a few bands can only capture limited information of such spectral features located in the red domain. Moreover, R_{rs} is essentially a nonlinear function of IOPs, which is due to the broadband effect of the optical attributes of IOPs (Vaillancourt et al., 2004; Zhou et al., 2012), leading to the signal overlap between adjacent bands. Therefore, the contributions to R_{rs} from the absorption or total backscattering coefficients of different water components can hardly be quantified by simply using linear operations. A logarithmic reconstruction model for R_{rs} inspired by its lognormal distribution is however more appropriate to interpret the strong covariation of R_{rs} at adjacent bands.

Five independent schemes listed in Table 3 were performed to verify the practical capability of the logarithmic and linear models. The band settings included two published schemes named C1 (710 nm was replaced with 700 nm here) and C2, referred to Lee et al. (2014) and Sathyendranath et al. (1989), as well as the spectral bands of MERIS,

Table 3
Band Placements of Referenced Schemes Together With MERIS, MODIS and GOCI bands in 400–700 nm

Band #	C1 ^a	C2 ^a	MERIS	MODIS	GOCI
1	400	400	412	412	412
2	425	410	443	443	443
3	445	420	490	488	490
4	460	440	510	531	555
5	475	480	560	547	660
6	495	500	620	667	680
7	515	510	665	678	
8	545	530	681		
9	565	540			
10	580	560			
11	605	580			
12	640	590			
13	665	630			
14	685	700			
15	700 (710)				

^aC1 and C2 are referred to Lee et al. (2014), Sathyendranath et al. (1989), respectively.

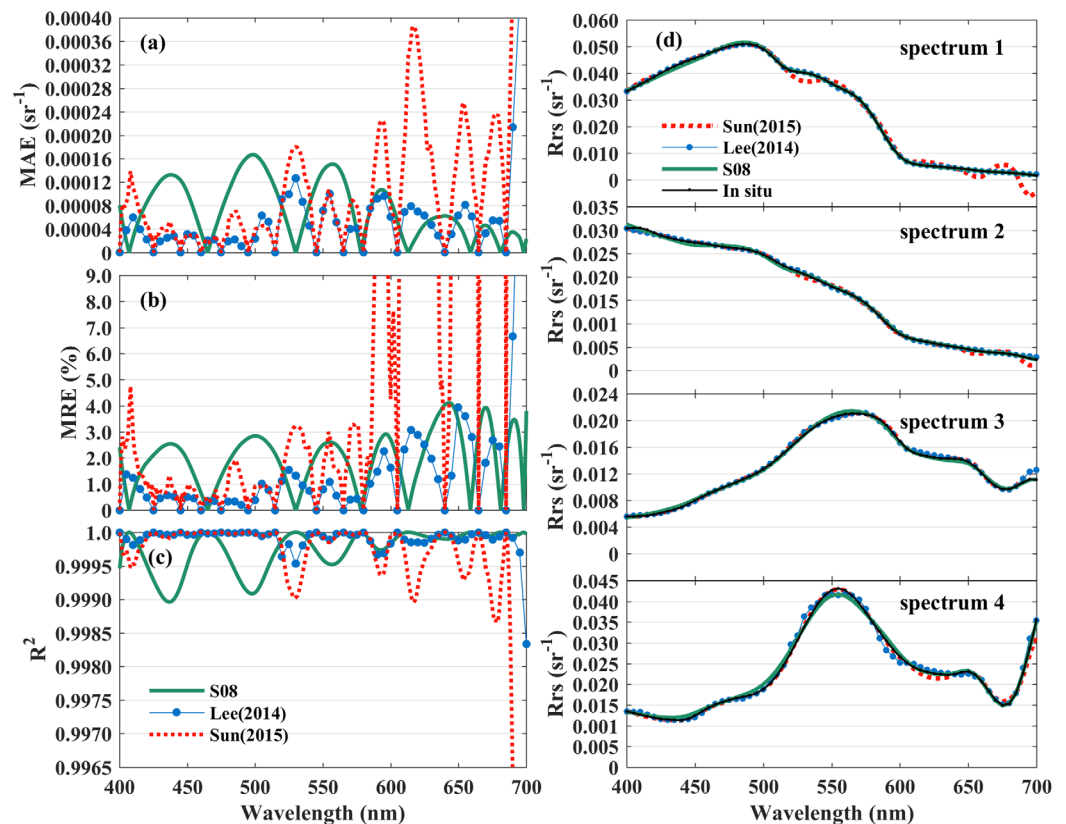


Figure 13. Distribution of (a) MAE, (b) MRE, (c) R^2 resulted from the three coefficient matrices of S08, Lee et al. (2014), and Sun et al. (2015) applied to validation data set, and (d) comparisons between four selected in situ R_{rs} spectra and the corresponding reconstructed R_{rs} spectra by the three algorithms.

MODIS and the Geostationary Ocean Color Imager (GOCI). The results in Figure 14 revealed that the statistical parameters generated by the two models were quite coincident when the input bands were sufficiently dense, such as in the range of 400–600 nm in C1 and C2. In addition, we found a remarkably improved performance for the logarithmic model in the red bands. This finding was more prominent when input bands were decreased, e.g., bands of MODIS and GOCI. We can conclude that the logarithmic model outperforms the linear model in terms of stability and flexibility in reconstructing hyperspectral R_{rs} and it has a great potential in providing reliable retrievals with a well-chosen scheme.

4.4. Interpretation for In Situ R_{rs} Uncertainties

The above analysis is based on the assumption that the in situ R_{rs} measurements are error-free, yet no absolutely accurate values for any in situ R_{rs} measurement in reality. But note that the established strategy in this study is still feasible and also of great significance for R_{rs} reconstruction. The uncertainties of in situ radiometric data were primarily influenced by (1) the measuring methods, such as the above-surface method and in-water profiling method, and (2) the natural conditions of environments, such as wind speed and cloud conditions. To reduce random uncertainties of in situ measurement in future, the observation data should be acquired by using single calibrated optical instrument under the same measurement protocol and post-process. On the other hand, the proposed R_{rs} reconstruction strategy in this study will not be almost affected by the in situ measurement, since its development is completely based on mathematical analysis method, and does not focus on the data source. Also, the uncertainties produced by our strategy are very weak, mostly in 1–5% range, which is roughly equivalent with in situ measurement errors in ideal conditions (Hooker & Maritorena, 2000; Qi et al., 2017). In short, more and more accurate in situ R_{rs} observations are always expected by the community, which will serve better for the R_{rs} reconstruction strategy. This work needs more effort in future.

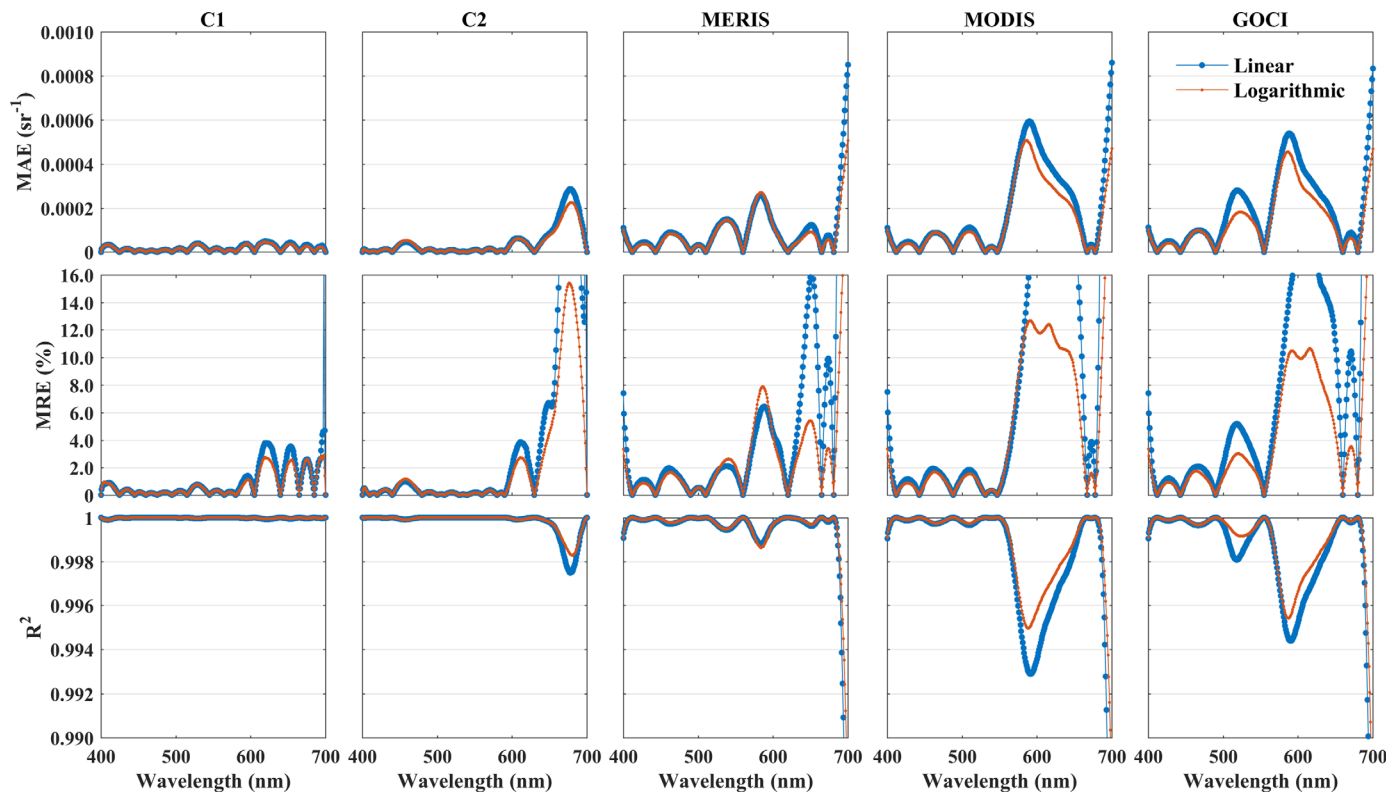


Figure 14. Comparison of the statistical parameters between linear and logarithmic model using five different band settings listed in Table 3, including two previously proposed schemes and spectral bands of MERIS, MODIS, and GOCI sensors within 400–700 nm. All in situ R_{rs} spectra were used.

4.5. Implication for Future Applications

The reconstruction method developed in the present study consists of two parts: the multi-band scheme (mainly, S08) and the logarithmic model. As we have discussed above, this method can retrieve missing R_{rs} data in the visible domain with high accuracy using eight-band measurements for global waters, indicating that S08 can serve as the optimal scheme. In terms of the sensor design, the performance of its preliminary application to HICO data implies that an optical sensor with the proposed eight bands can capture hyperspectral information by using this reconstruction method. Thus, the eight-band scheme can serve as a reference or an alternative choice for the band settings of future multiband sensors.

When data from a hyperspectral sensor or the eight-band scheme is not available, this method provides an alternative option for restoring R_{rs} with multi-bands on a specific satellite sensor. Since more algorithms have recently been specifically designed for existing satellite optical sensors (Hu et al., 2012; Qiu et al., 2017), this method also helps to generalize the algorithms by reconstructing spectra at identical bands for different sensors. Moreover, the method has provided a new insight for comparison of satellite-derived R_{rs} data from different sensors, and also benefits the radiometric calibration from the reconstructed full spectral data in the visible range.

It is however noteworthy that a comprehensive reconstruction method that can capture the full spectral information, such as chlorophyll fluorescence or absorption peaks by specific pigments (e.g., phycocyanin of cyanobacteria), is still a big challenge. For an improvement in the reconstruction method, extreme cases such as R_{rs} data from blooming waters should be included to further optimize the parameterization. It is also worthwhile to expand the spectral range of reconstruction from 400–700 nm to 350–800 nm including consideration for the atmospheric corrections and inversion algorithms of Chl-*a* and CDOM (IOCCG, 1998; Wei et al., 2016).

5. Conclusion

In the present study, a new reconstruction method for hyperspectral R_{rs} in the visible domain was proposed on the basis of extensive observations collected from various water environments including open ocean

waters, coastal waters and highly turbid inland waters. Ten alternative schemes were determined by the logarithmic model, with the number of the bands taken into account ranging from 6 to 15. The reconstruction accuracy decreased with reductions in the input band number, while the accuracy of first eight schemes met well the objective criterion introduced in this study. Generally, errors in the retrievals were lower than the uncertainties in the satellite-retrieved R_{rs} in blue bands. We also found that the logarithmic model outperformed the commonly used linear model due to its outstanding interpretation of the interdependence of R_{rs} for adjacent bands.

With thorough consideration of pros and cons, the eight-band scheme was ultimately selected for further comparative analysis. Results revealed that the parameterization derived by the eight-band scheme worked well for R_{rs} data in different water types. For an independent data set, the MAE and MRE values between in situ and reconstructed R_{rs} were generally $< 0.00016 \text{ sr}^{-1}$ and $< 3\%$ with $R^2 > 0.999$. The performance was also compared with a previously proposed linear model based on a 15-band scheme. Results implied that the eight-band scheme had great potential to be an optimal scheme as it contains only eight input bands but yields remarkable performance based on the logarithmic model.

In addition, a preliminary application of the eight-band scheme was performed on HICO-derived R_{rs} data at eight of the HICO bands, showing a promising perspective for further applications in optical satellite remote sensing. The reconstruction schemes presented in the study, especially the eight-band scheme, may provide significant implications for the future sensor design. In the meantime, our method plays an important role in discovering additional potential applications of satellite R_{rs} data and helps motivate the development and improvement of ocean color inversion algorithms.

Acknowledgments

This research was jointly supported by the National Key Research and Development Program of China (2016YFC1400901), the Jiangsu Provincial Programs for Marine Science and Technology Innovation (HY2017-5), the National Natural Science Foundation of China (41576172 and 41506200), the Provincial Natural Science Foundation of Jiangsu in China (BK20161532, BK20151526, BK20150914), the National Program on Global Change and Air-sea Interaction (GASI-03-03-01-01), the National Key R&D Program of China (2017YFB0503902), a project funded by "the Priority Academic Program Development of Jiangsu Higher Education Institutions (PAPD)", and the Canadian Space Agency Data Application and Utilization Program (DUAP). SeaBASS data can be downloaded from <https://seabass.gsfc.nasa.gov/>. In situ data supporting this article are available at <https://pan.baidu.com/s/1dGmUCvf>. We would like to thank two anonymous reviewers for their constructive comments and suggestions that improved the manuscript.

References

- Becker, B. L., Lusch, D. P., & Qi, J. (2005). Identifying optimal spectral bands from in situ measurements of Great Lakes coastal wetlands using second-derivative analysis. *Remote Sensing of Environment*, *97*, 238–248. <https://doi.org/10.1016/j.rse.2005.04.020>
- Campbell, J. W. (1995). The lognormal distribution as a model for bio-optical variability in the sea. *Journal of Geophysical Research*, *100*(C7), 13237–13254. <https://doi.org/10.1029/95JC00458>
- Craig, S. E., Jones, C. T., Li, W. K. W., Lazin, G., Horne, E., Caverhill, C., & Cullen, J. J. (2012). Deriving optical metrics of coastal phytoplankton biomass from ocean colour. *Remote Sensing of Environment*, *119*, 72–83. <https://doi.org/10.1016/j.rse.2011.12.007>
- Dekker, A. G., Malthus, T. J., Wijnen, M. M., & Seyhan, E. (1992). The effect of spectral band width and positioning on the spectral signature analysis of inland waters. *Remote Sensing of Environment*, *41*(2/3), 211–226. [https://doi.org/10.1016/0034-4257\(92\)90079-Y](https://doi.org/10.1016/0034-4257(92)90079-Y)
- Flink, P., Lindell, T., & Ostlund, C. (2001). Statistical analysis of hyperspectral data from two Swedish lakes. *Science of the Total Environment*, *268*(1), 155–169. [https://doi.org/10.1016/S0048-9697\(00\)00686-0](https://doi.org/10.1016/S0048-9697(00)00686-0)
- Gordon, H. R. (1979). Diffuse reflectance of the ocean: The theory of its augmentation by chlorophyll a fluorescence at 685 nm. *Applied Optics*, *18*(8), 1161–1166. <https://doi.org/10.1364/AO.18.001161>
- Gordon, H. R. (1997). Atmospheric correction of ocean color imagery in the Earth Observing System era. *Journal of Geophysical Research*, *102*(D14), 17081–17106. <https://doi.org/10.1029/96JD02443>
- Guanter, L., Kaufmann, H., Segl, K., Foerster, S., Rogass, C., Chabrilat, S., et al. (2015). The EnMAP spaceborne imaging spectroscopy mission for earth observation. *Remote Sensing*, *7*(7), 8830–8857. <https://doi.org/10.3390/rs70708830>
- Holden, H., & Ledrew, E. (1998). Spectral discrimination of healthy and non-healthy corals based on cluster analysis, principal components analysis, and derivative spectroscopy. *Remote Sensing of Environment*, *65*, 217–224. [https://doi.org/10.1016/S0034-4257\(98\)00029-7](https://doi.org/10.1016/S0034-4257(98)00029-7)
- Hooker, S. B., & Esaias, W. E. (1993). An overview of the SeaWiFS project. *Eos, Transactions American Geophysical Union*, *74*(21), 241–246. <https://doi.org/10.1029/93EO00945>
- Hooker, S. B., & Maritorena, S. (2000). An evaluation of oceanographic radiometers and deployment methodologies. *Journal of Atmospheric & Oceanic Technology*, *17*(6), 811–830. [https://doi.org/10.1175/1520-0426\(2000\)017<0811:AEORA>2.0.CO;2](https://doi.org/10.1175/1520-0426(2000)017<0811:AEORA>2.0.CO;2)
- Hu, C., Feng, L., & Lee, Z. (2013). Uncertainties of SeaWiFS and MODIS remote sensing reflectance: Implications from clear water measurements. *Remote Sensing of Environment*, *133*, 168–182. <https://doi.org/10.1016/j.rse.2013.02.012>
- Hu, C., Lee, Z., & Franz, B. (2012). Chlorophyll a algorithms for oligotrophic oceans: A novel approach based on three-band reflectance difference. *Journal of Geophysical Research*, *117*. C01011. <https://doi.org/10.1029/2011JC007395>
- Ibrahim, A., Franz, B., Ahmad, Z., Healy, R., & Gao, B.-C. (2018). Atmospheric correction for hyperspectral ocean color retrieval with application to the hyperspectral imager for the coastal ocean (HICO). *Remote Sensing of Environment*, *204*, 60–75. <https://doi.org/10.1016/j.rse.2017.10.041>
- IOCCG. (1998). Minimum requirements for an operational, ocean-colour sensor for the open ocean. In Morel, A. (Ed.), *Reports of the international ocean-colour coordinating group* (No. 1, pp. 1–50). Dartmouth, Canada: IOCCG.
- IOCCG. (1999). Status and plans for satellite ocean-colour missions: Considerations for complementary missions. In Yoder, J. A. (Ed.), *Reports of the international ocean-colour coordinating group* (No. 2, pp. 1–47). Dartmouth, Canada: IOCCG.
- Lee, C. M., Cable, M. L., Hook, S. J., Green, R. O., Ustin, S. L., Mandl, D. J., & Middleton, E. M. (2015). An introduction to the NASA Hyperspectral InfraRed Imager (HyspIRI) mission and preparatory activities. *Remote Sensing of Environment*, *167*, 6–19. <https://doi.org/10.1016/j.rse.2015.06.012>
- Lee, Z., & Carder, K. L. (2002). Effect of spectral band numbers on the retrieval of water column and bottom properties from ocean color data. *Applied Optics*, *41*(12), 2191–2201. <https://doi.org/10.1364/AO.41.002191>
- Lee, Z., Carder, K., Arnone, R., & He, M. (2007). Determination of primary spectral bands for remote sensing of aquatic environments. *Sensors*, *7*(12), 3428–3441. <https://doi.org/10.3390/s7123428>

- Lee, Z., Carder, K. L., & Arnone, R. A. (2002). Deriving inherent optical properties from water color: A multiband quasi-analytical algorithm for optically deep waters. *Applied Optics*, *41*(27), 5755–5772. <https://doi.org/10.1364/AO.41.005755>
- Lee, Z., Carder, K. L., Mobley, C. D., Steward, R. G., & Patch, J. S. (1998). Hyperspectral remote sensing for shallow waters. I. A semianalytical model. *Applied Optics*, *37*(27), 6329–6338. <https://doi.org/10.1364/AO.37.006329>
- Lee, Z., Carder, K. L., Mobley, C. D., Steward, R. G., & Patch, J. S. (1999). Hyperspectral remote sensing for shallow waters. 2. Deriving bottom depths and water properties by optimization. *Applied Optics*, *38*(18), 3831–3843. <https://doi.org/10.1364/AO.38.003831>
- Lee, Z., Pahlevan, N., Ahn, Y.-H., Greb, S., & O'donnell, D. (2013). Robust approach to directly measuring water-leaving radiance in the field. *Applied Optics*, *52*(8), 1693–1701. <https://doi.org/10.1364/AO.52.001693>
- Lee, Z., Shang, S., Hu, C., & Zibordi, G. (2014). Spectral interdependence of remote-sensing reflectance and its implications on the design of ocean color satellite sensors. *Applied Optics*, *53*(15), 3301–3310. <https://doi.org/10.1364/AO.53.003301>
- Lubac, B., & Loisel, H. (2007). Variability and classification of remote sensing reflectance spectra in the eastern English Channel and southern North Sea. *Remote Sensing of Environment*, *110*(1), 45–58. <https://doi.org/10.1016/j.rse.2007.02.012>
- Lucke, R. L., Corson, M., McGlothlin, N. R., Butcher, S. D., Wood, D. L., Korwan, D. R., et al. (2011). Hyperspectral Imager for the Coastal Ocean: Instrument description and first images. *Applied Optics*, *50*(11), 1501–1516. <https://doi.org/10.1364/AO.50.001501>
- Matsuoka, A., Babin, M., & Devred, E. C. (2016). A new algorithm for discriminating water sources from space: A case study for the southern Beaufort Sea using MODIS ocean color and SMOS salinity data. *Remote Sensing of Environment*, *184*, (August), 124–138. <https://doi.org/10.1016/j.rse.2016.05.006>
- Mélin, F., & Sclap, G. (2015). Band shifting for ocean color multi-spectral reflectance data. *Optics Express*, *23*(3), 2262–2279. <https://doi.org/10.1364/OE.23.002262>
- Moisan, J. R., Moisan, T. A. H., & Linkswiler, M. A. (2011). An inverse modeling approach to estimating phytoplankton pigment concentrations from phytoplankton absorption spectra. *Journal of Geophysical Research*, *116*, C09018. <https://doi.org/10.1029/2010JC006786>
- Mueller, J. L. (1976). Ocean color spectra measured off the Oregon coast: Characteristic vectors. *Applied Optics*, *15*(2), 394–402. <https://doi.org/10.1364/AO.15.000394>
- Pope, R. M., & Fry, E. S. (1997). Absorption spectrum (380–700 nm) of pure water II Integrating cavity measurements. *Applied Optics*, *36*(33), 8710–8723. <https://doi.org/10.1364/AO.36.008710>
- Qi, L., Lee, Z., Hu, C., & Wang, M. (2017). Requirement of minimal signal-to-noise ratios of ocean color sensors and uncertainties of ocean color products. *Journal of Geophysical Research: Oceans*, *122*, 1–17. <https://doi.org/10.1002/2016JC012558>. Received
- Qiu, Z. (2013). A simple optical model to estimate suspended particulate matter in Yellow River Estuary. *Optics Express*, *21*(23), 27891–27904. <https://doi.org/10.1364/OE.21.027891>
- Qiu, Z., Xiao, C., Perrie, W., Sun, D., Wang, S., Shen, H., et al. (2017). Using Landsat 8 data to estimate suspended particulate matter in the Yellow River estuary. *Journal of Geophysical Research: Oceans*, *122*, 276–290. <https://doi.org/10.1002/2016JC012412>
- Sathyendranath, S., Hoge, F. E., Platt, T., & Swift, R. N. (1994). Detection of phytoplankton pigments from ocean color: Improved algorithms. *Applied Optics*, *33*(6), 1081–1089. <https://doi.org/10.1364/AO.33.001081>
- Sathyendranath, S., Prieur, L., & Morel, A. (1989). A three-component model of ocean colour and its application to remote sensing of phytoplankton pigments in coastal waters. *International Journal of Remote Sensing*, *10*(8), 1373–1394. <https://doi.org/10.1080/01431168908903974>
- Siswanto, E., Tang, J., Yamaguchi, H., Ahn, Y. H., Ishizaka, J., Yoo, S., et al. (2011). Empirical ocean-color algorithms to retrieve chlorophyll-a, total suspended matter, and colored dissolved organic matter absorption coefficient in the Yellow and East China Seas. *Journal of Oceanography*, *67*(5), 627–650. <https://doi.org/10.1007/s10872-011-0062-z>
- Spitzer, D., & Wernand, M. R. (1986). Assessment of solar irradiance spectra. *Applied Optics*, *25*(15), 2466–2467. <https://doi.org/10.1364/AO.25.002466>
- Sun, D. Y., Hu, C. M., Qiu, Z. F., & Wang, S. Q. (2015). Reconstruction of hyperspectral reflectance for optically complex turbid inland lakes: Test of a new scheme and implications for inversion algorithms. *Optics Express*, *23*(11), 718–740. <https://doi.org/10.1364/oe.23.00a718>
- Tool, D. A., & Siegel, D. A. (2001). Modes and mechanisms of ocean color variability in the Santa Barbara Channel. *Journal of Geophysical Research*, *106*(C11), 26985–27000. <https://doi.org/10.1029/2000JC000371>
- Tsai, F., & Philpot, W. (1998). Derivative analysis of hyperspectral data. *Remote Sensing of Environment*, *66*, 41–51. [https://doi.org/10.1016/S0034-4257\(98\)00032-7](https://doi.org/10.1016/S0034-4257(98)00032-7)
- Vaillancourt, R. D., Brown, C. W., Guillard, R. R. L., & Balch, W. M. (2004). Light backscattering properties of marine phytoplankton: Relationships to cell size, chemical composition and taxonomy. *Journal of Plankton Research*, *26*(2), 191–212. <https://doi.org/10.1093/plankt/fbh012>
- Wang, G., Lee, Z., Mishra, D. R., & Ma, R. (2016). Retrieving absorption coefficients of multiple phytoplankton pigments from hyperspectral remote sensing reflectance measured over cyanobacteria bloom waters. *Limnology and Oceanography: Methods*, *14*(7), 432–447. <https://doi.org/10.1002/lom3.10102>
- Wei, J., Lee, Z., Ondrusek, M., Mannino, A., Tzortziou, M., & Armstrong, R. (2016). Spectral slopes of the absorption coefficient of colored dissolved and detrital material inverted from UV-visible remote sensing reflectance. *Journal of Geophysical Research: Oceans*, *121*, 1953–1969. <https://doi.org/10.1002/2015JC011415>
- Werdell, P. J., & Bailey, S. W. (2002). The seawifs Bio-Optical Archive and Storage (SeaBASS): Current architecture and implementation. In Fargion, G. S. & McClain, C. R. (Eds.), (NASA Tech. Memo., TM-2002–211617, pp. 1–45). Greenbelt, MD: NASA Goddard Space Flight Cent.
- Werdell, P. J., Franz, B. A., Bailey, S. W., Feldman, G. C., Boss, E., Brando, V. E., et al. (2013). Generalized ocean color inversion model for retrieving marine inherent optical properties. *Applied Optics*, *52*(10), 2019–2037. <https://doi.org/10.1364/AO.52.002019>
- Wernand, M. R., Shimwell, S. J., & DeMunck, J. C. (1997). A simple method of full spectrum reconstruction by a five-band approach for ocean colour applications. *International Journal of Remote Sensing*, *18*(9), 1977–1986. <https://doi.org/10.1080/014311697217981>
- Xi, H., Hieronymi, M., Röttgers, R., Krasemann, H., & Qiu, Z. (2015). Hyperspectral differentiation of phytoplankton taxonomic groups: A comparison between using remote sensing reflectance and absorption spectra. *Remote Sensing*, *7*, 14781–14805. <https://doi.org/10.3390/rs71114781>
- Xi, H., & Zhang, Y. (2011). Total suspended matter observation in the Pearl River estuary from in situ and MERIS data. *Environmental Monitoring and Assessment*, *177*, 563–574. <https://doi.org/10.1007/s10661-010-1657-3>
- Zhang, H., Qiu, Z., Sun, D., Wang, S., & He, Y. (2017). Seasonal and interannual variability of satellite-derived chlorophyll-a (2000–2012) in the Bohai Sea, China. *Remote Sensing*, *9*(6), 582–596. <https://doi.org/10.3390/rs9060582>
- Zhou, W., Wang, G., Sun, Z., Cao, W., Xu, Z., Hu, S., & Zhao, J. (2012). Variations in the optical scattering properties of phytoplankton cultures. *Optics Express*, *20*(10), 11189. <https://doi.org/10.1364/OE.20.011189>